Hindawi
Adsorption Science & Technology
Volume 2021, Article ID 9290644, 12 pages
https://doi.org/10.1155/2021/9290644

Research Article

Photocatalytic Degradation of Methylene Blue and Antibacterial Activity of Mesoporous TiO_2-SBA-15 Nanocomposite Based on Rice Husk

Eid H. Alosaimi,[1] Ibrahim Hotan Alsohaimi,[2] Talal E. Dahan,[3] Qiao Chen,[4] Ayman Abdelaziz younes,[1] Belal El-Gammal,[1] and Saad Melhi[1]

[1]*Department of Chemistry, College of Science, University of Bisha, P.O. Box 511, Bisha 61922, Saudi Arabia*
[2]*Chemistry Department, College of Science, Jouf University, Sakaka 2014, Saudi Arabia*
[3]*Department of Biology, College of Science, University of Bisha, P.O. Box 511, Bisha 61922, Saudi Arabia*
[4]*Chemistry Department, School of Life Sciences, Sussex University, Brighton BN1 9QJ, UK*

Correspondence should be addressed to Ibrahim Hotan Alsohaimi; ehalshaimi@ju.edu.sa

Received 11 August 2021; Revised 20 August 2021; Accepted 5 September 2021; Published 20 September 2021

Academic Editor: Silvano Mignardi

Concerns have been increased regarding the existence of pollutants in environmental water resources and their risks to the ecosystem and human society. TiO_2 photocatalyst is considered as an effective photocatalyst to remove the pollutants. Herein, the mesoporous TiO_2-SBA-15 was prepared using the rice husk extract as the silica source. The fabricated nanocomposites were characterized using FTIR, small and wide angle XRD, Raman spectroscopy, UV-vis, BET surface area analysis, and HRTEM. The photocatalytic efficiency of the composites for the degradation of methylene blue (MB) has been evaluated under UV irradiation. Interestingly, due to the excellent dispersion of TiO_2 on the wall of SBA-15 and good hydrophilicity, the nanocomposites displayed a good catalytic activity. The higher photodegradation performance was achieved by the composite containing 10 wt% TiO_2 by which the MB was fully degraded within 15-20 min of irradiation. Besides, TiO_2-SBA-15 could effectively inhibit the growth of Gram-positive and Gram-negative bacteria. These results offer a practical and economic approach in the environmental management industries.

1. Introduction

Rice husk (RH) is a byproduct of rice production [1–3]. RH contributes approximately 20-25 wt % of the whole dry weight of rice [4]. With the annual rice production of 489.1 million tons [5], about 120 million tons of RH were produced as the biomass waste. Due to its weak mechanical strength, poor nutritional value, and low bulk density, the use of RH is limited [6–8]. So far, the most popular RH disposal approach is the open field burning which leads to air pollution, greenhouse gas emissions, and a waste of energy [9]. However, RH contains a high amount of silica, which could be used as the raw material for producing value-added silicon-based materials with interesting texture and morphology. The implementations of such substances stemming from rice husks are very inclusive [10, 11]. In the past decade, this research area has been dramatically progressed and extended, driven by the worldwide emphasis on sustainable and renewable resources.

As a chemically inert material, porous silica plays a significant role in various applications including adsorption, sensing, and catalyst support and templating, owing to its high surface area, adjustable porosity, and surface properties [12–14]. Its application largely depends on its morphology and microstructure. Mesoporous silica can be artificially synthesized with a certain degree of control in its nanomorphology [15]. However, it usually involves a complicated process, for instance, high quality of the amorphous silica was produced by the multistep thermal reduction of crude silica. The need for high temperatures and high pressure

under extreme acidic condition is energy-intensive with high impact on the environment [16]. Hence, it is important to develop an affordable, sustainable, and environmentally friendly technique for the fabrication of porous silica to satisfy the rising demand for its widespread applications.

With the rapid population and industrialization growth, water pollution from organic contaminants seems to have become a big worldwide problem that risks the ecological system and human health [17, 18]. To remove organic contaminants from water, several physical and biological treatment approaches have been used, including ultrafiltration, coagulation, and adsorption [19, 20]. However, their practical applications are restricted by the limited capacity to remove trace organic compounds and the costs involved in the replacement of media. Therefore, a highly efficient, environmentally friendly, and sustainable water treatment process is needed to remove organic pollutants from water.

Due to the moderate operating conditions, high catalytic activity, and environmentally safe, TiO_2 photocatalyst has been an excellent candidate for the removing of organic contaminants from air and water [21, 22]. Although the use of TiO_2 nanoparticles is valuable for scientific research, the size of the particles restricts their practical use in water treatment. It is difficult and expensive to recover and resue the TiO_2 nanoparticles from a liquid environment. Meanwhile, complex water matrices could easily interfere with the surface property of the suspended fine TiO_2 particles [23]. Therefore, the design and producing of nanoporous TiO_2 framework have attracted some attention [24–26]. In such case, porous silica, as an optically transparent material, is an ideal candidate for supporting TiO_2 used as the photocatalyst in an aqueous environment.

The primary target of the present work is to develop an effective, economical, and sustainable nanocomposite of TiO_2 supported by mesoporous nanosilica using the rice husk as the sustainable raw material. The catalytic efficiency of the composites for the photocatalytic degradation of methylene blue (MB) was evaluated under UV irradiation. The unique mesoporous nanocomposite material displayed excellent photocatalytic performance in the degradation of MB and the bacteria inhabitation tests. The immobilized TiO_2 also showed success in the recovering and reusing process with the potential for practical environmental treatment.

2. Materials and Methods

2.1. Materials. Sodium hydroxide (NaOH, ≥99%), hydrogen peroxide solution (H_2O_2, 30 wt %), titanium isopropoxide (TTIP, 99%), the nonionic surfactant of $EO_{20}PO_{70}EO_{20}$, (Pluronic P123), ethanol (99%), and hydrochloric acid (HCl, 37%) were procured from Sigma-Aldrich Co., USA. MB (>96%) was supplied from Central Drug House (P) Ltd., India. H_2SO_4 (96%) used for silica extraction was obtained from Fisher Scientific. Rice husk was obtained by removing rice. Deionized water was utilized in the whole experiment. All materials were used without any further treatment.

2.2. Material Fabrication

2.2.1. Extraction of Nanosilica from Rice Husk. Silica was extracted from rice husk according to the previously reported procedure [27]. Briefly, 150 g of ground husk and 60 ml of concentrated H_2SO_4 were added in a glass bottle containing 1 L of deionized water. The mixture was digested at 80°C for 4 h under mechanical stirring. The precipitate was then collected by filtration. The obtained raw silica was calcinated at 800°C for 3 h to remove residual impurity. Finally, the produced silica was bleached using 10% H_2O_2 solution at room temperature for 3 hours.

2.2.2. Preparation of SBA-15. Mesoporous SBA-15 silica was synthesized using sodium silicate solution with Pluronic 123 as the structure-directing agent under acidic conditions. The Pluronic 123 solution was made by dissolving 4 g of Pluronic 123 in 120 g of HCl (2 M), followed by stirring at 40°C until Pluronic 123 was completely dissolved. Sodium silicate solution was produced by dissolving 1 g SiO_2 from the rice husk in 230 M NaOH solution (3 M). The P-123 solution was gradually added to the sodium silicate solution at 40°C under intense stirring. The reaction between the P123 polymer micelles and the sodium silicate produced the emulsion after rapid mixing [28]. The mixture was continuously stirred for 24 h at 40°C, and the SBA-15 precipitates were formed. The solid was separated by filtration and rinsed several times with a mixture of water and ethanol. Finally, the solid sample was dried at 80°C under vacuum for 12 h. The collected SBA-15 was calcined for 6 h at 600°C to remove any organic residuals (Scheme 1).

2.2.3. Preparation of TiO_2-SBA-15 Nanocomposite. TTIP was used as the Ti precursor. In a typical synthesis, 1.0 g of dried SBA-15 was dispersed in 50 ml of ethanol followed by sonication for 60 min. Various amounts of TTIP (corresponding to 5, and 10 wt% TiO_2) were then introduced to the suspension. The mixture was mixed for another 60 min until a clear solution was formed. Then, a certain volume of deionized water (30 ml) was introduced dropwise under vigorous stirring for 4 h to hydrolyze the TTIP to Ti $(OH)_4$ species and to be deposited on the surface of SBA-15. The solid product was separated, rinsed several times with H_2O and ethanol, dried overnight at 120°C, and finally calcinated for 4 h at 400°C to create the TiO_2-SBA-15 nanocomposites [29, 30] (Scheme 1).

2.3. Material Characterization. Small and wide angle X-ray diffraction (XRD) measurements were carried out using an X-ray diffractometer (XPERT, PANalytical) with Cu Kα ($\lambda = 0.154$ nm) radiation at 40 mA and 40 kV using a secondary monochromator. The surface texture and N_2-isotherms were obtained using a BET surface analyzer (NOVA 3200, Quantachrome Instruments) at 77 K. The pore size distribution was evaluated from the adsorption branch of the nitrogen isotherms employing the Barrett–Joyner–Halenda (BJH) model. The samples were activated for 3 hours prior to analysis at 250°C. The Brunauer–Emmett–Teller (BET) model was used to compute the surface areas. High-resolution images of the nanostructures were collected

Scheme 1: The fabrication strategies for TiO_2-SBA-15 nanocomposite from rice husk.

Table 1: Unit cell parameter and texture characteristics of pristine SBA-15 and TiO_2-SBA-15 nanocomposite containing various TiO_2 contents.

Sample	TiO_2 loading[a] (wt%)	TiO_2 loading[b] (wt%)	a_0/nm[a]	A_{BET}/(m^2g^{-1})[b]	V_P/(cm^3/g)[c]	D_P/Ads/nm[d]	W/(nm)[e]	E_g /eV
SBA-15	—	—	14.43	869	1.24	5.7	6.28	—
5%TiO_2-SBA-15	5	4.54	15.05	702	1.13	6.4	6. 40	3.09
10%TiO_2-SBA-15	10	9.73	16.51	695	0.95	5.5	7.40	3.01

[a]TiO_2 concentration in the gel. [b]TiO_2 concentration in the calcined materials measured by ICP.

using a high-resolution transmission electron microscope (HRTEM, JEM-1230, JEOL) operating at 200 kV. A droplet of a colloid solution containing the sample in ethanol was applied to a carbon-coated copper grid and allowed to dry in air at ambient temperature. FT-IR spectra were recorded using a Fourier transform infrared spectrophotometer (IR Tracer-100, Shimadzu). The diffractograms were performed in the 2Θ range of 0.5 to 3° (low angle) and 10-80° (wide angle) with step size of 0.01° and 10 s per step. The Raman spectra were recorded on a high-performance Raman analyzer (ProRaman-L, Enwave Optronics) using a doubled Nd:YAG laser ($\lambda = 532$ nm) as the excitation laser. With a laser power of 10 mW, the beam of laser was concentrated on a 0.10 mm diameter point on the nanocomposite.

The optical property was measured with a UV-vis spectrophotometer (UV-2600, Shimadzu) equipped with diffuse reflectance difference spectroscopy attachment (DRDS). The sample was spread on a glass slide with a certain thickness, d. The measurement was performed at ambient temperature. The absorption coefficient $\alpha(\nu)$ was calculated using Eq. (1):

$$\alpha(\nu) = \frac{1}{d} \log\left(\frac{Io}{I}\right), \quad (1)$$

where I_0 and I are the intensities of the incident and transmitted light, respectively. The optical bandgap (E_g) was obtained from the absorption coefficient $\alpha(\nu)$ using Eq. (2)

$$\alpha h\nu = [B(h\nu - Eg)]^r, \quad (2)$$

where h_ν is the photon energy of the incident light, and B is the band tailing constant. The value of r is ½ or 2 for direct or indirect bandgap [31]. To obtain the bandgap energy value, the Tauc plots were created by plotting $(\alpha h\nu)^{1/2}$ against $(h\nu)$.

The chemical oxygen demand (COD) was measured using an oxidation method in the presence of $K_2Cr_2O_7$ [32].

2.4. Photodegradation Performance Measurements. In a typical photodegradation experiment, in double wall jacket glass reactor for temperaure controler, 50 mg of TiO_2-SBA-15 photocatalyst was added in 100 ml MB solution with initial concentration ($C_o = 4 \times 10^{-5}$ mol/l). To achieve the adsorption-desorption equilibrium, the mixture solution was stirred in the dark for 30 min before the UV irradiation. The quantity of adsorbed MB was evaluated employing Eq. (3).

$$qt = \frac{(Co - Ce)V}{m}, \quad (3)$$

where q_t is the adsorption capacity, and m is the weight of the catalyst. C_o and C_e are the original and equilibrium weight volume concentrations of the MB. V is the total volume of the MB solution. The suspension was then placed vertically under a UV (UVA, 365 nm, 10 W) equiped with optical transimisssion filter. The distance between the glass reactor and the lamp is 25 cm for all experiments. Every 5 min during the photoirradiation, 5 ml of MB solution was collected. The solid nanocomposite was removed by centrifuge, and the concentration of the MB was determined by the UV–vis spectrometer. The MB photodegradation performance was explored by analyzing the kinetic data from the reduction of the MB concentration. All performance measurements were carried out in triplicate.

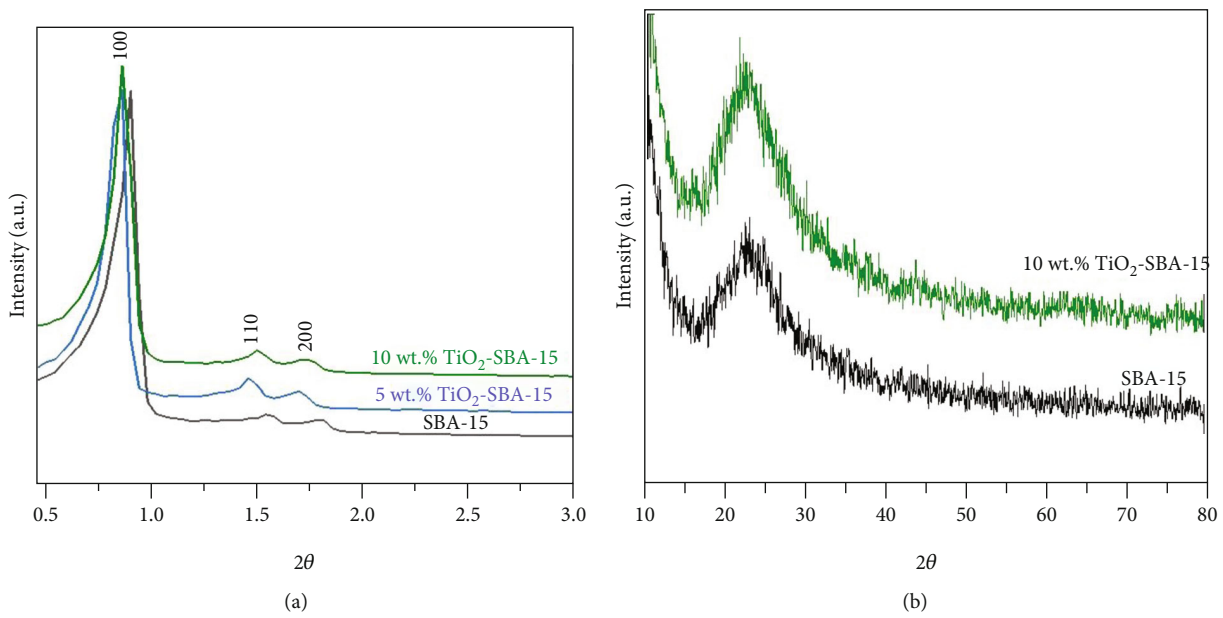

FIGURE 1: (a) Low-angle XRD and (b) wide-angle XRD patterns of pure SBA-15 and TiO_2-SBA-15 nanocomposite (JCPDS card no. 21-1272 (anatase TiO_2) and ICDD # 00-001-0424 (silica phase)).

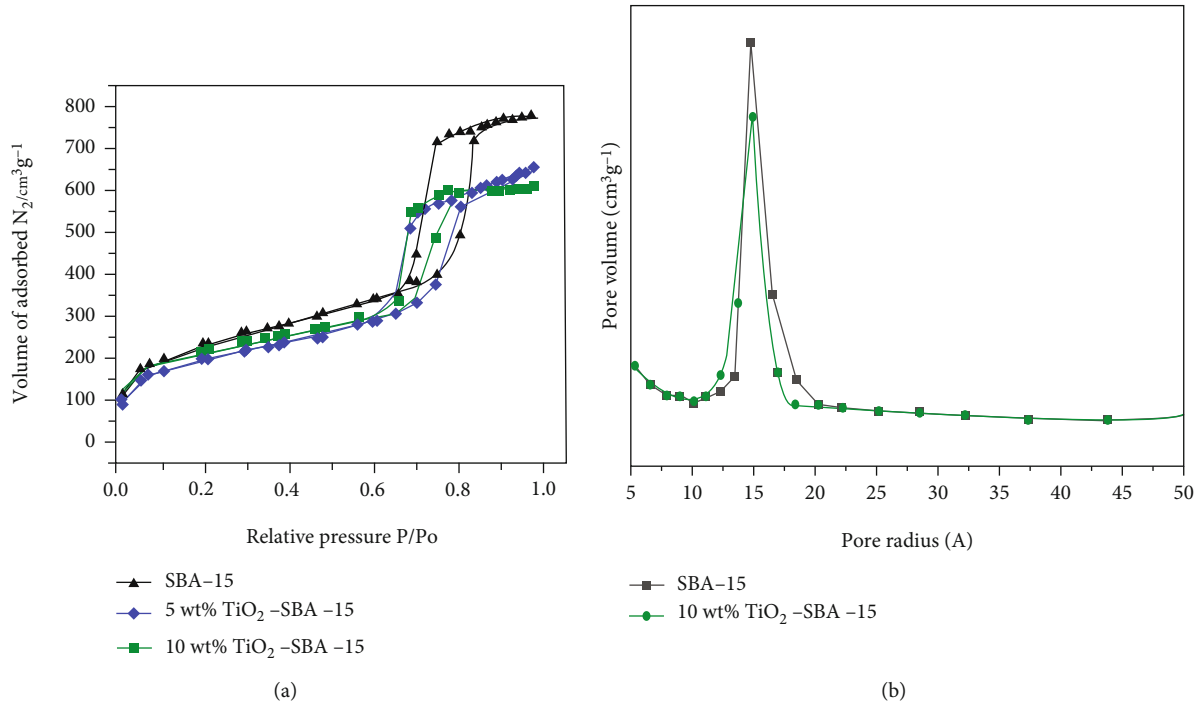

FIGURE 2: (a) Nitrogen adsorption/desorption isotherms and pore size distribution of pure SBA-15 and TiO_2-SBA-15 nanocomposite containing various TiO_2 contents. (b) Pore size distributions for SBA-15 and TiO_2-SBA-15 (10 wt % TiO_2).

2.5. Antibacterial Performance. The antibacterial performance of the fabricated materials was performed by the agar well diffusion approach. The bacterial isolates were cultured for 20 hours at 35°C in a medium of nutritional broth having 10 g/L NaCl, 3 g/L extract of yeast, and 8 g/L bactotryptone. Using sterile cotton buds, 100 μl of the suspensions of the cell was dispersed on a nutrient agar surface, and the agar was pierced with 8 mm diameter reservoirs and loaded with 300 μl of TiO_2-SBA-15 aqueous solutions (5 mg/ml). The plates was incubated for 24 h at 35°C. The antibacterial performance of the nanocomposite was assessed by the size of the inhibition zone (growth diameter). The antibacterial performance of TiO_2-SBA-15 nanocomposite with 10 wt % TiO_2 against Gram-positive and Gram-negative bacteria is

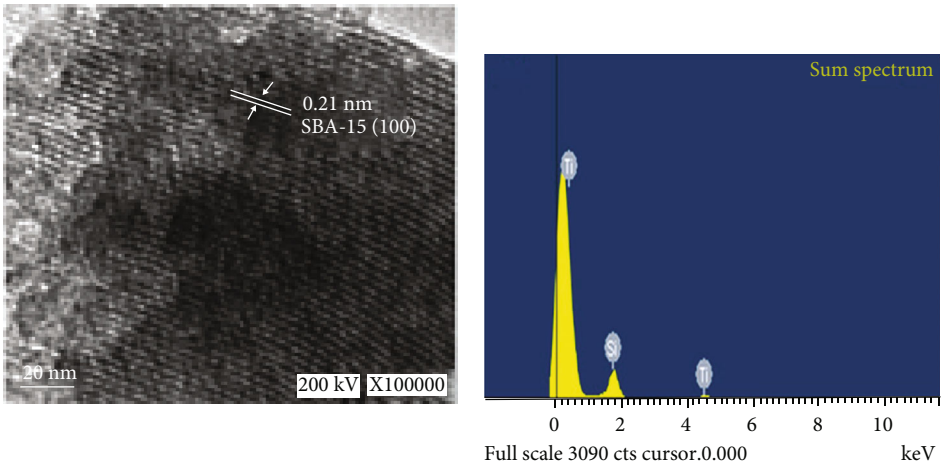

Figure 3: (a) HRTEM images and (b) EDS of 10 wt % TiO_2-SBA-15 nanocomposite.

tested, and four different bacteria were selected for testing, including B. subtilis, B. cereus, Klebsiella pneumonia, and E. coli.

3. Results and Discussion

3.1. Material Characterization. In order to examine the TiO_2 loadings in the composite of X%TiO_2-SBA-15, elemental analysis is used, and the results are reported in Table 1. The results revealed that the TiO_2 loadings in the composites range from 4.5 to 9.7 wt%.

The small-angle XRD patterns for pristine SBA-15 and TiO_2-SBA-15 nanocomposites with different TiO_2 contents are presented in Figure 1(a). All the fabricated composites display well-defined XRD diffraction peaks related to the (1 0 0), (1 1 0), and (2 0 0) crystal planes of the SBA-15 structure with P6mm hexagonal symmetry [33]. The high intensities of these diffraction peaks indicate that good quality SBA-15 mesostructure was successfully produced. With the incorporating of TiO_2, the diffraction peaks from the SBA-15 shift towards smaller angles, representing the increased lattice constant for the SBA-15. This finding suggests that some of the Si^{4+} were substituted by the Ti^{4+} since Si^{4+} has a radius of 0.040 nm, smaller than that of the Ti^{4+} (0.061 nm). The unit cell parameter ($a_o = 2d_{100}/\sqrt{3}$). of the prepared composite has increased upon the incorporation with TiO_2 (Table 1) and increased with increase TiO_2 content. In general, isomorphous replacement of Si^{4+} by Ti^{4+} ions helps to create an atomically tight interface between the TiO_2 and SiO_2, which is important for the stability of the composite materials. It also implies the excellent penetration of TiO_2 into the SBA-15 wall structures of the pores. The appearance of the XRD peaks from SBA-15 with similar intensities and peak width after TiO_2 coating suggests that the SBA-15 crystal structures were preserved during the TiO_2 coating. Figure 1(b) displays the wide-angle XRD patterns of pure SBA-15 and TiO_2-SBA-15 composite with 10 wt % TiO_2. The weak wide peak centered at $2\theta = 22°$ is associated with the amorphous silica (ICDD # 00-001-0424 (silica phase)). No diffraction peaks belong to TiO_2 were

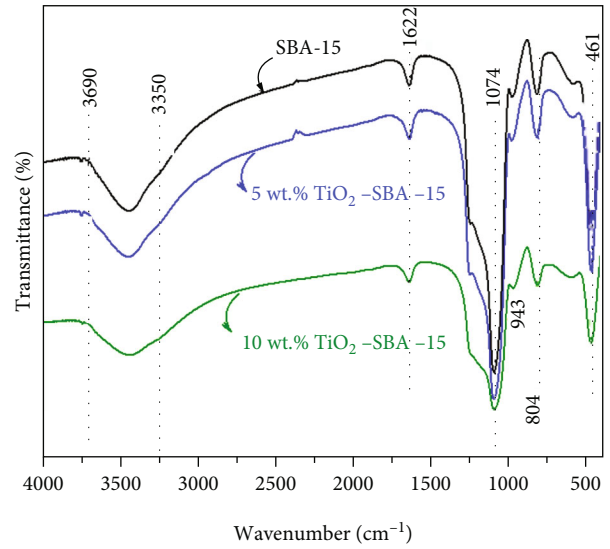

Figure 4: FTIR spectra of pure SBA-15 and TiO_2-SBA-15 nanocomposite containing various TiO_2 contents.

observed (JCPDS card no. 21-1272 (anatase TiO_2)), suggesting that a well-dispersed thin layer of TiO_2 coating was formed within the SBA-15 matrix.

Figure 2 shows the nitrogen adsorption/desorption isotherms and pore size distribution of pristine SBA-15 and TiO_2-SBA-15 nanocomposite with various TiO_2 contents (5 and 10 wt.%). The measured properties of the synthesized materials are summarized in Table 1, including the specific surface area (A_{BET}), the total pore volume (V_p), the average pore diameter (D_p), the wall thickness (W), and the bandgap energy (E_g). The lattice constant was calculated from the XRD diffraction angle. The surface area was determined based on the BET isotherm. The pore structure was obtained using the BJH model. The wall thickness was calculated by ($a_o - D_p$). The bandgap energy was calculated from the UV-vis absorption spectra, as discussed below.

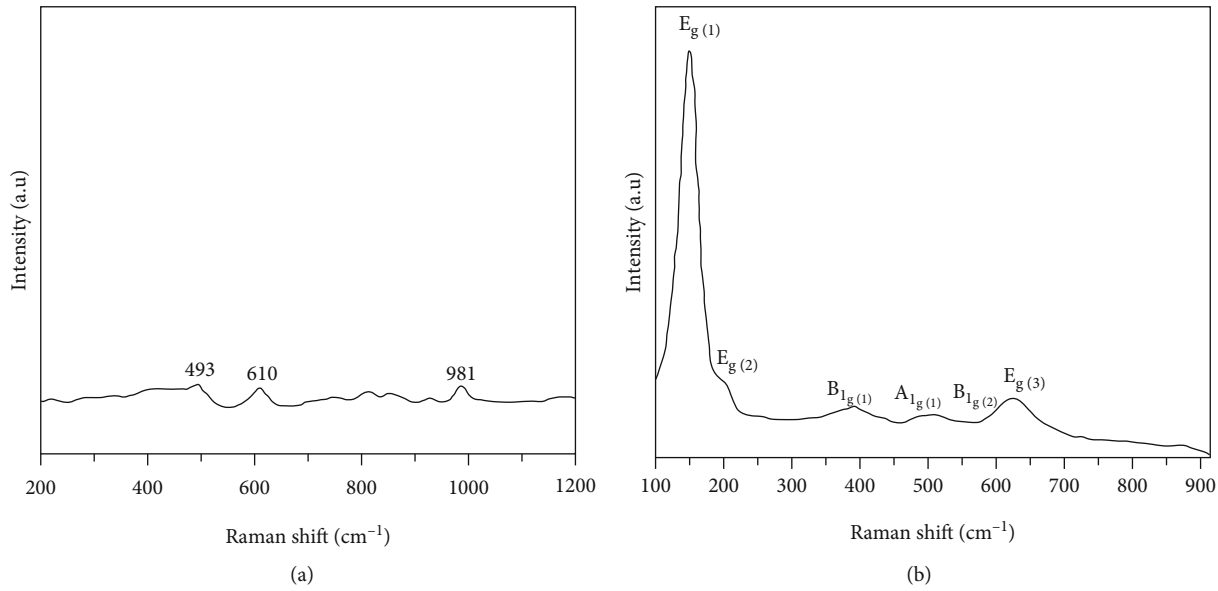

Figure 5: Raman spectrum of (a) SBA-15 and (b) 10 wt % TiO_2-SBA-15 nanocomposite.

The isotherms in Figure 2(a) show the representative type IV, with wide H1 type hysteresis loop, which is common for the mesoporous materials [34]. Each isotherm shows a sharp increase of the adsorbed N_2 volume, and characteristic of the capillary condensation within mesopores occurs for a relative pressure P/P_o larger than 0.62. This jump is irreversible, which forms a hysteresis loop with parallel desorption and adsorption branches (type H1). The sharpness of this jump indicates the uniformity of mesopore sizes. The similar isotherm curvatures between SBA-15 and TiO_2-SBA-15 suggest that they both have the hexagonally arranged mesopores linked by smaller micropores [35]. The surface area of the TiO_2-SBA-15 with 10 wt % TiO_2 is 695 m^2/g with the pore diameter of 5.5 nm and pore volume of 0.95 cm^3/g (Table 1). With the increase in the TiO_2 loading, the wall thickness of TiO_2-SBA-15 was increased due to the TiO_2 that was incorporated on both inside and outside of the SiO_2 pores. Moreover, all materials have similar pore sizes with narrow pore size distributions as calculated from the adsorption branch of the nitrogen isotherms using the Barrett–Joyner–Halenda (BJH) method, shown in Figure 2(b). Hence, there is a slightly collapse of the porous SBA-15 structure during the TiO_2 incorporation. The data is consistent with the findings from the XRD and HRTEM studies.

To verify the mesoporous structure of the SBA-15 after TiO_2 coating, HRTEM images for TiO_2-SBA-15 nanocomposite with 10 wt % TiO_2 are displayed in Figure 3. HRTEM image of 10 wt % TiO_2-SBA-15 nanocomposite with uniform one-dimensional mesochannels, parallel, and hexagona mesostructure has developed. A d value 0.21 nm corresponds to the (100) lattice plane of SBA-15 that was observed, indicating that the SBA mesoporous structure was maintained after the integration of TiO_2 in the SBA-15 matrix, which is in good agreement with the XRD results.

The FT-IR spectra of synthesized SBA-15 and TiO_2-SBA-15 nanocomposite with various TiO_2 contents are depicted in Figure 4. There are bands representative of hydroxylated silica in the FTIR spectrum of SBA-15: 1074, 943, 804, 555, and 461 cm^{-1}. The bands at 1074 and 804 cm^{-1} ascribed to the Si–O–Si bond's asymmetric and symmetric stretching vibrations, respectively. The bands at 943 and 461 cm^{-1} relate to the Si–OH and Si–O–Si bonds'-bending vibrations [36, 37]. The existence of a characteristic absorption band at 555 cm^{-1} attributable to Si–O–Si symmetric modes of the silicon-oxygen tetrahedral is a distinguishing characteristic of this spectrum. Bending vibrations of coordinately attached and adsorbed water molecules are shown by the bands at 3454 and 1622 cm^{-1}. We find a decrease in the intensity of the absorption bands for stretching vibrations of the Si–O–Si bond in the spectrum of the composite with SBA-15 majority, and their maximum is moved toward smaller frequencies compared to the SBA-15 spectrum. We find a reduction in the intensity of the absorption bands for Si–O–Si stretching vibrations and a shift in their maximum to lower frequencies as the quantity of TiO_2 in the composite increases. Simultaneously, with a high silica content in the composite, the absorption band corresponding to Ti-O vibration of octahedraon TiO_6 vanishes. This could be linked to the transition of titanium atoms from octahedral to tetrahedral coordination when they substitute silicon in the SiO_4^{-4} tetrahedron [37]. We can only explain the absorption in this area as a result of the distinctive vibrations of Si–O–Ti bonds following suitable thermal treatment of the materials because the absorption bands for the Si–OH and Si–O–Ti bonds are near.

Raman spectroscopy was performed to explore the structural changes upon TiO_2 deposition within the SBA-15 matrix and also to identify the phase of the developed titania. The Raman spectra of SBA-15 and 10 wt% TiO_2-SBA-15 nanocomposite are displayed in Figure 5. SBA-15 in Figure 5(a) displays a band about 493 cm^{-1}, which is ascribed to tetrasiloxane rings. The bands about 610 and

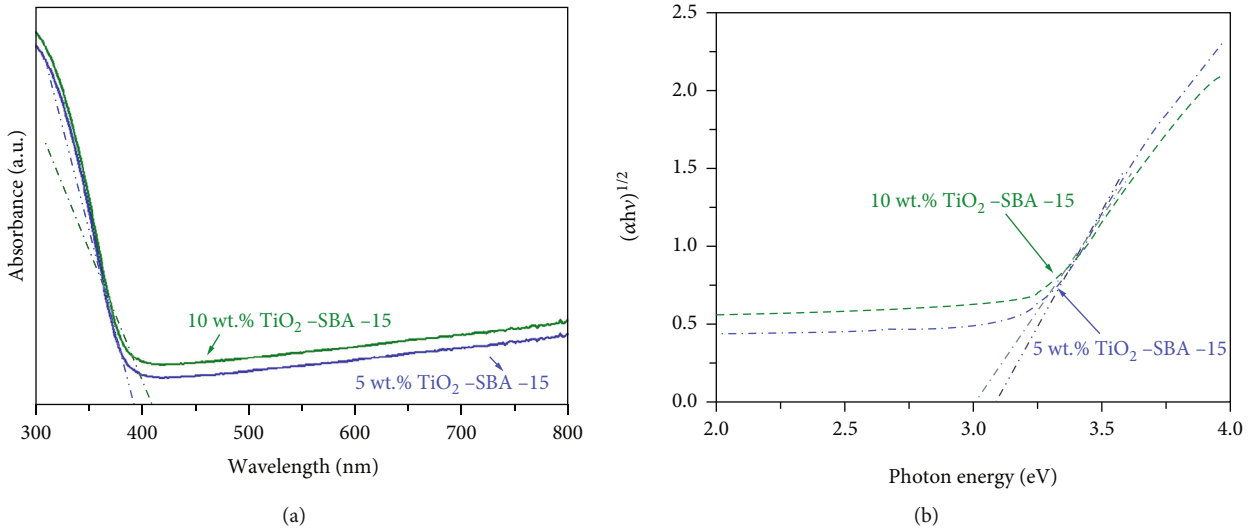

FIGURE 6: UV–vis absorption spectra (a) and Tauc's profile for the band gap determination (b) of TiO_2-SBA-15 nanocomposite containing various TiO_2 contents.

981 cm^{-1} could be attributed to cyclic trisiloxane rings and the Si–OH stretching vibration, respectively. Figure 5(b) shows the Raman spectrum of 10 wt % TiO_2-SBA-15 nanocomposite. Four Raman active bands were identified at 149, 410, 510, and 633 cm^{-1}, respectively, which are assigned to the Eg, B1g, A1g/B1g, and Eg bands associated with the anatase phase. Furthermore, the SBA-15 band is nearly undetectable, implying the presence of highly dispersed TiO_2 species within the SBA-15.

UV-vis absorption measurements were conducted to explore the optical properties of the TiO_2-SBA-15 composites at different TiO_2 loadings. The recorded spectra of the TiO_2-SBA-15 nanocomposite with 5 and 10 wt % TiO_2 are displayed in Figure 6. The TiO_2-SBA-15 composites mainly absorb the UV, shown in Figure 6(a). The edge of the absorption shifted to a longer wavelength at higher TiO_2 content [38, 39]. To determine the bandgap energies of the prepared nanocomposites, the corresponding Tauc's plots are produced in Figure 6(b). Bandgap energies were obtained by extrapolating the linear part of the plot to the *x*-axis. Their values are summarized in Table 1. It can be seen that the bandgap value was slightly larger for the sample with 5 wt % TiO_2 (3.09 eV) than that for the sample with 10 wt % of TiO_2 (3.01 eV). This observation is likely due to that at lower TiO_2 loading, and the size of the TiO_2 nanoparticles within the mesoporous is decreased as compared to that at higher TiO_2 loading. Moreover, the bandgap energy is affected by the quantum confinement and increases as the particles size decreases [40, 41].

3.2. Catalytic Performance. The dark adsorption experiments of MB over pure SBA-15 and TiO_2-SBA-15 nanocomposite with 5 and 10 wt.% TiO_2 at different time intervals are displayed in Figure 7. The adsorption saturations were achieved around 30 mins for all samples with the adsorption capacities of 11.8, 7.3, and 4.1 mg/g for pure SBA-15 and TiO_2-SBA-15 nanocomposite with 5 and 10 wt.% TiO_2, respectively. Hence, the photocatalytic decomposition experiments were delayed

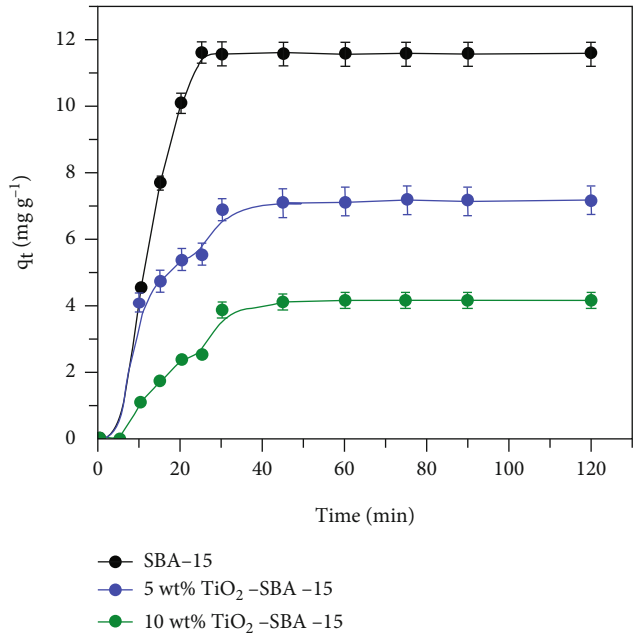

FIGURE 7: Time-dependent adsorption behavior of the MB on TiO_2-SBA-15 nanocomposite containing various TiO_2 contents under dark condition.

by 30 mins after mixing, allowing the adsorption equilibrium to be achieved. Owing to the large surface area of the mesoporous silica matrix, the SBA-15 displayed the highest adsorption capacity. However, after TiO_2 incorporation, the adsorption capacity during the dark experiments was decreased compared to pure SBA-15, possibly due to the clogging and the decrease in surface area. The sample with 10 wt % of TiO_2 offered the lowest adsorption capacity.

Under the UV irradiation, the MB photocatalytic degradation by the TiO_2-SBA-15 nanocomposites with 5 and 10 wt % TiO_2 was examined. The findings are displayed in

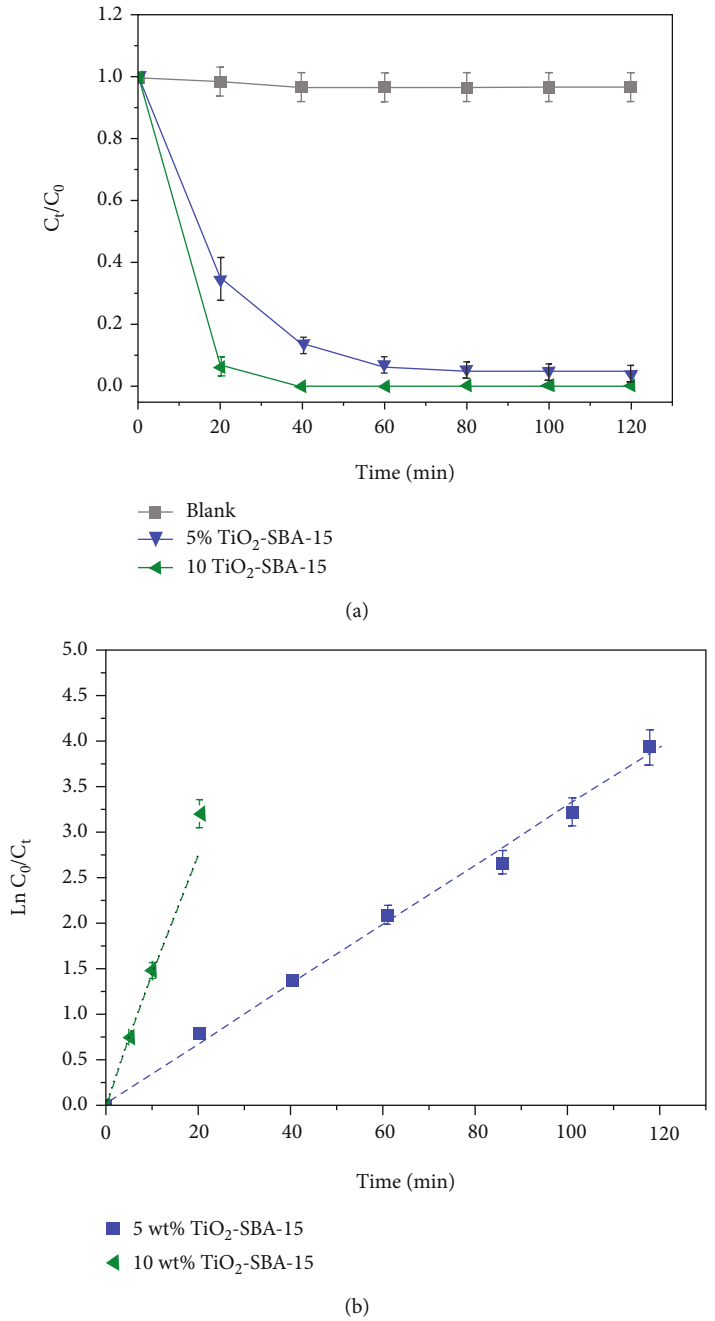

Figure 8: (a) Photocatalytic activity and (b) first-order kinetic curve under UV irradiation of TiO_2-SBA-15 nanocomposites.

Table 2: Chemical oxygen demand (COD) decline of MB with respect to time over the 10 wt% TiO_2-SBA-15 nanocomposite.

Physicochemical parameters	Prephotocatalytic degradation	After dark for 30 min	Postphotocatalytic degradation after				
			20 min	40 min	60 min	80 min	120 min
COD (mg/L)	34.8 ± 0.6	14.3 ± 0.4	11.3 ± 0.3	10.1 ± 0.5	9.3 ± 0.2	5.1 ± 0.2	2.2 ± 0.1

Figure 8 and Table 2. To identify the effects of UV on the MB molecule, a control experiment using 100 ml MB solution under UV irradiation without catalyst was carried out, shown in Figure 8(a). Only a limited degradation of MB (< 2%) was observed. Hence, the MB is stable under UV irradiation. The photocatalytic performance under UV irradiation of the nanocomposites with different TiO_2 loadings for the degradation of MB dye is also shown in Figure 8(a), plotted with the normalized MB concentrations as a function of reaction time. The higher photodegradation

performance was achieved by the composite containing 10 wt% TiO_2 by which the MB was fully degraded within 15-20 min of irradiation. To measure the reaction rate constant, a first-order kinetic model was used. Figure 8(b) shows the logarithm of MB relative concentration as a function of time. The degradation process obeys the first-order kinetic. The TiO_2-SBA-15 photocatalyst with 10 wt % TiO_2 gives an MB degradation rate constant of 0.139 min^{-1}, which is about 4 times more efficient than that with 5 wt % TiO_2 loading (0.033 min^{-1}). Therefore, the rate constant was improved by the increase of the TiO_2 loading. As a control experiment, 10% TiO_2-SBA-15 was fabricated using SBA-15 (Sigma-Aldrich) as a support. A comparatively decline in the photocatalytic corresponding to rate constat ($k = 0.114$ min^{-1}) was achieved when using commercial SBA-15 as a support. The photocatalytic performance is determined by the density of the surface catalytic center, the reactant adsorption capacity, and light absorption efficiency. At different TiO_2 loadings, there is no significant difference in the BET-specific surface area. The TiO_2-SBA-15 with 10 wt % of TiO_2 showed lower adsorption capacity for the MB than that with 5 wt % of TiO_2, which is possibly resulted from the reduced BET surface area and pore volume. Such character should result in a lower reaction rate constant, which is contradictory to the kinetic measurement results. More importantly, the bandgap energy of the TiO_2-SBA-15 with 5 wt % of TiO_2 is about 3.09 eV, which is much shorter than the wavelength of the photocatalysis excitation source (365 nm). Hence, it is expected that the TiO_2-SBA-15 with 5 wt % of TiO_2 would have much lower excitation efficiency. The smaller TiO_2 particle size in the TiO_2-SBA-15 with 5 wt % of TiO_2 also implies a higher density of surface defects, which can behave like charge recombination centers. Therefore, the dominate effects that determining the photocatalytic performance are the matching of the bandgap energy with the excitation light source, while the crystal quality also affected the charge recombination [42–46].

Based on the abovementioned findings, TiO_2-SBA-15 nanocomposite had an uniform pore distribution and large surface area, which aided the MB uptake and diffusion by the SBA-15 mesochanel, resulting in MB accumulation surrounding the TiO_2 nanoparticles. This near vicinity between MB and the active centers is likely crucial to increasing the degradation performance. The nanocomposite particles were photoexcited that generate electron (e^-) and (h). The electron participates in the reduction processes, whereas holes participate in the oxidation processes. The following equations display the mechanism of the photocatalytic reaction [47].

$$
\begin{aligned}
TiO_2 - SBA - 15\ UV &\longrightarrow {}^{h^+}VB + e^-{}_{CB},\\
O_2 + e^- &\longrightarrow {}\cdot O_2^-,\\
H_2O + h^+ &\longrightarrow {}\cdot OH + H^+,\\
\cdot O_2^- + H_2O &\longrightarrow {}\cdot HO_2 + OH^-,\\
\cdot HO_2 + H_2O &\longrightarrow H_2O_2 + \cdot OH,\\
H_2O_2 &\longrightarrow 2\cdot OH,\\
\cdot OH + MB &\longrightarrow \text{decomposition product} + CO_2.
\end{aligned}
\tag{4}
$$

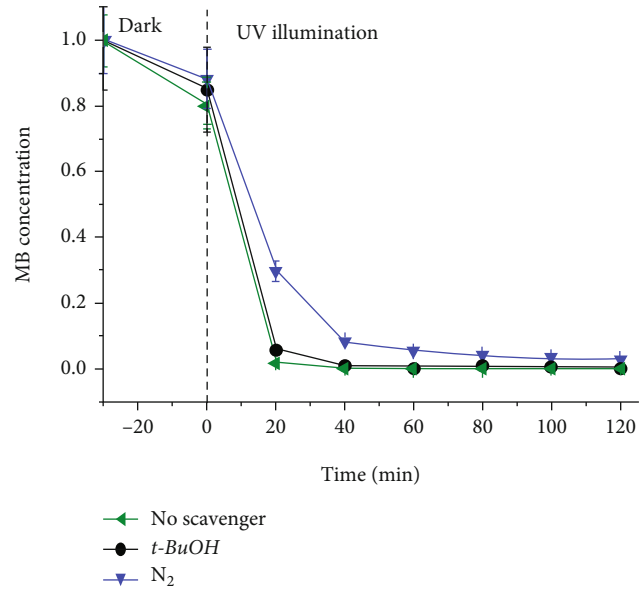

Figure 9: MB degradation using the 10% TiO_2-SBA-15 nanocomposite without scavenger and with scavengers under UV-light irradiation.

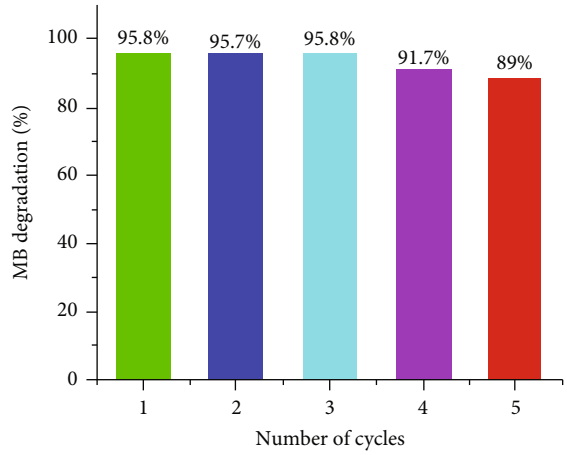

Figure 10: Durability of 10% TiO_2-SBA-15 nanocomposites towards the photodegradation activity of MB.

Table 3: Antibacterial activity of SBA-15 and 10 wt% TiO_2-SBA-15 nanocomposite against Gram-positive and Gram-negative bacteria.

Bacteria	Kind	Diameter of inhibition zone (mm)	
		SBA-15	10 wt % TiO_2-SBA-15
B. subtilis	+ve	20.3 ± 0.67	26.1 ± 0.44
B. cereus	+ve	17.1 ± 0.43	27.2 ± 0.51
K. pneumoniae	-ve	20.1 ± 0.36	31.3 ± 0.33
E. coli	-ve	24.3 ± 0.17	30.1 ± 0.87

The involvement of active species was investigated using a trapping experiment to reveal the photodegradation mechanism of MB. Tertiary butyl alcohol (t-BuOH) was used to scavenge ·OH, while nitrogen bubbling was employed to

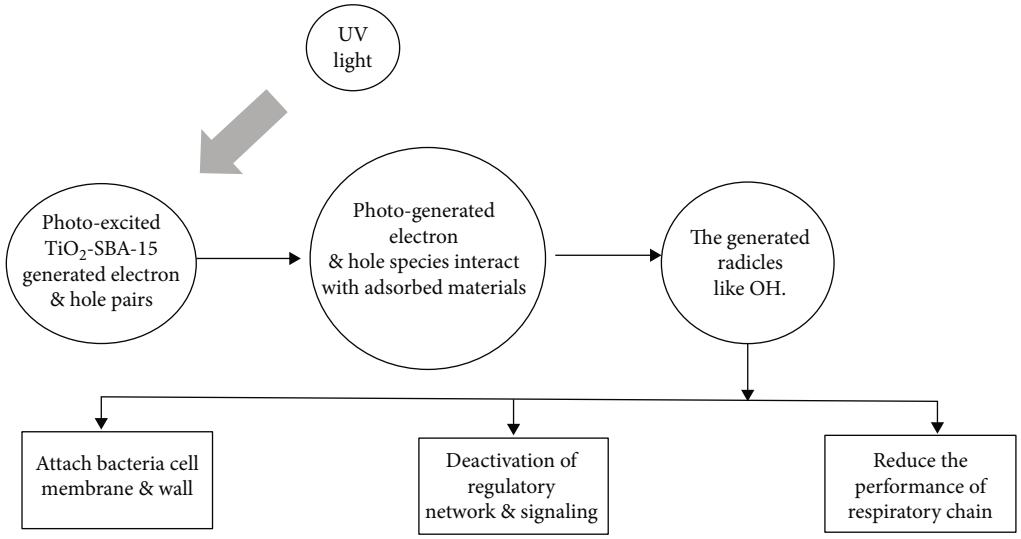

Scheme 2: The antibacterial performance-based mechanism.

scavenge $\cdot O_2-$ and h+. Figure 9 demonstrates that adding *t-BuOH* has minimal effect on MB degradation, indicating that ·OH is not involved in the photodegradation process, whereas the N_2 bubbling dramatically reduces MB removal, suggesting that h + and $\cdot O_2-$ are the key active species in MB degradation.

Furthermore, to ensure dye degradation, a chemical oxygen demand (COD) experiment was carried out. The COD test is a popular method for determining the organic strength of wastewater [32]. The test allows for waste assessment in terms of total oxygen needed for the organic matter oxidation to CO_2 and water. A significant decrease in COD indicates degradation in carbon content in the sample and so indicates the extent of mineralization. Organic carbon is converted to gaseous CO_2 as a result of degradation. The COD was substantially lowered (Table 2) as a result of the oxidative mineralization process, which involved the aromatic rings opening with the transitory synthesis of carboxylic acids, followed by the evolution of CO_2 via the "photo-Kolbe" reaction.

$$R - COO^- + h^+ \longrightarrow R^\bullet + CO_2. \quad (5)$$

With the use of a 10% TiO_2-SBA-15 nanocomposite, the dye molecules might be totally mineralized, based on the considerable reduction in COD values.

One of the advantages of heterogeneous catalysis is the ability to recycle and reutilize the catalysts with a relatively simple procedure at low cost if the catalytic performance of the catalysts can be maintained. To evaluate the recyclability of the TiO_2-SBA-15 with 10 wt % TiO_2, the used catalyst was collected and immediately reused in the MB degradation without further treatment. The catalytic kinetic data for the consecutive five cycles are presented in Figure 10. The results show that the degradation performance values were 95.8, 95.7, 95.8, 91.7, and 89%. After the fifth degradation run, the ICP and surface area were tested. Obvious, no remarkable TiO_2 is detected after the fifth run in reaction mixture, suggesting that the leaching process is not responsible for the decrease in the performance. However, the measured surface area after the fifth run for the nanocomposite is decreased ($673\ m^2\ g^{-1}$), which is the main reason for the decrease the catalytic degradation.

The antibacterial performance of TiO_2-SBA-15 nanocomposite with 10 wt % TiO_2 against Gram-positive and Gram-negative bacteria is presented in Table 3. Four different bacteria were selected for testing, including B. subtilis, B. cereus, Klebsiella pneumonia, and E. coli. For both Gram-positive and Gram-negative bacteria, to acquire a better understanding of the antibacterial performance, a few control studies were carried out. The antibacterial performance of the nanocomposite-free control sample was tested under the identical conditions and found no significant differences. Besides, the antibacterial performance of the SBA-15 was also tested to enable the comparison with the nanocomposite prepared in this work. A comparatively decline in the antibacterial activity was achieved when using SBA-15. Particularly, the highest antibacterial activity was observed for the TiO_2 deposited nanoparticles. Thanks to the presence of TiO_2, the 10 wt% TiO_2-SBA-15 nanocomposites display an enhanced antibacterial performance. Hence, the photocatalyst offered an effective universal antibacterial activity [48]. Bacteria possess enzymatic antioxidant protective mechanisms that limit lipid per oxidation as well as the impacts OH_2^- and ·OH radicals. When such components are surpassed, a series of redox processes can cause the death of a cell by changing many critical components likes DNA, cell membrane, cell wall, and metabolism pathways. The mechanism of antibacterial performance of TiO_2-SBA-15 nanocomposite was presented in Scheme 2.

4. Conclusion

Mesoporous SBA-15 nanomaterial is successfully synthesized using sustainable, low-cost, and environmentally friendly rice husk extract as the silica source and used as the support for TiO_2 nanoparticles. With 10 wt% loading

of TiO_2, the TiO_2-SBA-15 nanocomposite showed higher efficiency in the reduction of MB within 15-20 min of irradiation and excellent antibacterial performance. This could be attributed to the excellent light absorption and limited density of surface defects. The degradation process of 5 and 10 wt % TiO_2-SBA-15 obeys the first-order kinetic with rate constant of 0.139 min^{-1} and 0.033 min^{-1}, respectively. The TiO_2-SBA-15 nanocomposite also shows excellent recyclability with long lasting catalytic performance. Therefore, TiO_2-SBA-15 is a potential excellent photocatalyst for practical application in environmental treatment.

Data Availability

The data used to support the findings of this study are included within the article.

Conflicts of Interest

The authors declare that they have no conflict of interest.

Acknowledgments

The authors extend their appreciation to the Deputyship for Research & Innovation, Ministry of Education in Saudi Arabia for funding this research work through the project number (UB-35-1442).

References

[1] J. Yu, J. B. Zhang, J. He, Z. D. Liu, and Z. N. Yu, "Combinations of mild physical or chemical pretreatment with biological pretreatment for enzymatic hydrolysis of rice hull," *Bioresource Technology*, vol. 100, no. 2, pp. 903–908, 2009.

[2] E. Cabane, X. Zhang, K. Langowska, C. G. Palivan, and W. Meier, "Stimuli-responsive polymers and their applications in nanomedicine," *Biointerphases*, vol. 7, no. 1, p. 9, 2012.

[3] M. Balamurugan and S. Saravanan, "Producing nanosilica from *Sorghum vulgare* seed heads," *Powder Technology*, vol. 224, pp. 345–350, 2012.

[4] F. W. Chang, M. T. Tsay, and M. S. Kuo, "Effect of thermal treatments on catalyst reducibility and activity in nickel supported on RHA-Al_2O_3 systems," *Thermochimica Acta*, vol. 386, no. 2, pp. 161–172, 2002.

[5] X. Zhang, Y. Shen, X. Y. Yu, and X. J. Liu, "Dissipation of chlorpyrifos and residue analysis in rice, soil and water under paddy field conditions," *Ecotoxicology and Environmental Safety*, vol. 78, pp. 276–280, 2012.

[6] D. F. Houston, *Rice: Chemistry and Technologh*, American Association of Cereal Chemists, Inc., St Paul, MN, 1972.

[7] M. Fang, L. Yang, G. Chen, Z. Shi, Z. Luo, and K. Cen, "Experimental study on rice husk combustion in a circulating fluidized bed," *Fuel Processing Technology*, vol. 85, no. 11, pp. 1273–1282, 2004.

[8] S. V. Efremova, "Rice hull as a renewable raw material and its processing routes," *Russian Journal of General Chemistry*, vol. 82, no. 5, pp. 999–1005, 2012.

[9] J. S. Lim, Z. Abdul Manan, S. R. Wan Alwi, and H. Hashim, "A review on utilisation of biomass from rice industry as a source of renewable energy," *Renewable and Sustainable Energy Reviews*, vol. 16, no. 5, pp. 3084–3094, 2012.

[10] G. A. Habeeb and H. B. Mahmud, "Study on properties of rice husk ash and its use as cement replacement material," *Materials Research*, vol. 13, no. 2, pp. 185–190, 2010.

[11] L. Sun and K. Gong, "Silicon-based materials from rice husks and their applications," *Industrial & Engineering Chemistry Research*, vol. 40, no. 25, pp. 5861–5877, 2001.

[12] F. P. Glasser, *Silica in encyclopedia of materials science and engineering*, The MIT Press, Cambridge, Massachusetts, 1986.

[13] S. Uhrlandt, *Silica in Kirk-Othmer encyclopedia of chemical technology*, John Wiley & Sons, Inc., Hoboken, New Jersey, 2006.

[14] J. L. Gurav, I. K. Jung, H. H. Park, E. S. Kang, and D. Y. Nadargi, "Silica aerogel: synthesis and applications," *Journal of Nanomaterials*, vol. 2010, Article ID 409310, 11 pages, 2010.

[15] Y. Wang, N. Su, L. Ye et al., "Tuning enantioselectivity in asymmetric hydrogenation of acetophenone and its derivatives via confinement effect over free-standing mesoporous palladium network catalysts," *Journal of Catalysis*, vol. 313, pp. 113–126, 2014.

[16] W. Li, J. Cao, W. Xiong et al., "In-situ growing of metal-organic frameworks on three-dimensional iron network as an efficient adsorbent for antibiotics removal," *Chemical Engineering Journal*, vol. 392, article 124844, 2020.

[17] Y. Yang, G. Zeng, D. Huang et al., "In situ grown single-atom cobalt on polymeric carbon nitride with bidentate ligand for efficient photocatalytic degradation of Refractory antibiotics," *Small*, vol. 16, no. 29, article 2001634, 2020.

[18] S. Chen, D. Huang, G. Zeng et al., "In-situ synthesis of facet-dependent $BiVO_4$/Ag_3PO_4/PANI photocatalyst with enhanced visible-light-induced photocatalytic degradation performance: synergism of interfacial coupling and hole-transfer," *Chemical Engineering Journal*, vol. 382, article 122840, 2020.

[19] L. Lei, D. Huang, C. Zhang, R. Deng, S. Chen, and Z. Li, "F dopants triggered active sites in bifunctional cobalt foam toward electrocatalytic overall water splitting in neutral and alkaline media: Experiments and theoretical calculations," *Journal of Catalysis*, vol. 385, pp. 129–139, 2020.

[20] W. Xiong, Z. Zeng, G. Zeng et al., "Metal-organic frameworks derived magnetic carbon- $\alpha Fe/Fe_3C$ composites as a highly effective adsorbent for tetracycline removal from aqueous solution," *Chemical Engineering Journal*, vol. 374, pp. 91–99, 2019.

[21] M. Jiménez-Tototzintle, I. J. Ferreira, S. da Silva Duque, P. R. Guimarães Barrocas, and E. M. Saggioro, "Removal of contaminants of emerging concern (CECs) and antibiotic resistant bacteria in urban wastewater using UVA/TiO_2/H_2O_2 photocatalysis," *Chemosphere*, vol. 210, pp. 449–457, 2018.

[22] T. Fotiou, T. M. Triantis, T. Kaloudis, K. E. O'Shea, D. D. Dionysiou, and A. Hiskia, "Assessment of the roles of reactive oxygen species in the UV and visible light photocatalytic degradation of cyanotoxins and water taste and odor compounds using C-TiO_2," *Water Research*, vol. 90, pp. 52–61, 2016.

[23] O. Autin, J. Hart, P. Jarvis, J. MacAdam, S. A. Parsons, and B. Jefferson, "The impact of background organic matter and alkalinity on the degradation of the pesticide metaldehyde by two advanced oxidation processes: UV/H_2O_2 and UV/TiO_2," *Water Research*, vol. 47, no. 6, pp. 2041–2049, 2013.

[24] M. J. Arlos, M. M. Hatat-Fraile, R. Liang et al., "Photocatalytic decomposition of organic micropollutants using immobilized TiO_2 having different isoelectric points," *Water Research*, vol. 101, pp. 351–361, 2016.

[25] M. Anpo, H. Nakaya, S. Kodama, Y. Kubokawa, K. Domen, and T. Onishi, "Photocatalysis over binary metal oxides. Enhancement of the photocatalytic activity of titanium dioxide in titanium-silicon oxides," *The Journal of Physical Chemistry*, vol. 90, no. 8, pp. 1633–1636, 1986.

[26] A. Staykov, E. P. Ferreira-Neto, J. M. Y. S. Cruz, S. Ullah, and U. P. Rodrigues-Filho, "The stability of titania-silica interface," *International Journal of Quantum Chemistry*, vol. 118, no. 4, article e25495, 2018.

[27] D. Battegazzore, S. Bocchini, J. Alongi, and A. Frache, "Rice husk as bio-source of silica: preparation and characterization of PLA–silica biocomposites," *RSC Advances*, vol. 4, no. 97, pp. 54703–54712, 2014.

[28] D. Zhao, Q. Huo, J. Feng, B. F. Chmelka, and G. D. Stucky, "Nonionic triblock and star diblock copolymer and oligomeric surfactant syntheses of highly ordered, hydrothermally stable, mesoporous silica structures," *Journal of the American Chemical Society*, vol. 120, no. 24, pp. 6024–6036, 1998.

[29] I. Fatimah, A. Said, and U. A. Hasanah, "Preparation of TiO2-SiO2 using rice husk ash as silica source and the kinetics study as photocatalyst in methyl violet decolorization," *Bulletin of Chemical Reaction Engineering & Catalysis*, vol. 10, no. 1, pp. 43–49, 2015.

[30] I. Fatimah, N. I. Prakoso, I. Sahroni et al., "Physicochemical characteristics and photocatalytic performance of TiO_2/SiO_2 catalyst synthesized using biogenic silica from bamboo leaves," *Heliyon*, vol. 5, no. 11, article e02766, 2019.

[31] L. Singh, V. Thakur, R. Punia, R. Kundu, and A. Singh, "Structural and optical properties of barium titanate modified bismuth borate glasses," *Solid State Sciences*, vol. 37, pp. 64–71, 2014.

[32] R. Jain and S. Sikarwar, "Removal of hazardous dye congored from waste material," *Journal of Hazardous Materials*, vol. 152, no. 3, pp. 942–948, 2008.

[33] J. S. Beck, J. C. Vartuli, W. J. Roth et al., "A new family of mesoporous molecular sieves prepared with liquid crystal templates," *Journal of the American Chemical Society*, vol. 114, no. 27, pp. 10834–10843, 1992.

[34] K. S. W. Sing, D. H. Everett, R. A. W. Haul et al., "Reporting physisorption data for gas/solid systems with special reference to the determination of surface area and porosity (Recommendations 1984)," *Pure and Applied Chemistry*, vol. 57, no. 4, pp. 603–619, 1985.

[35] M. Imperor-Clerc, P. Davidson, and A. Davidson, "Existence of a microporous corona around the mesopores of silica-based SBA-15 materials templated by triblock copolymers," *Journal of the American Chemical Society*, vol. 122, no. 48, pp. 11925–11933, 2000.

[36] N. A. Chumaevskii, *Vibrational Spectra of Heteroorganic Compounds of Group IV-B and V-B Elements*, Nauka, Moscow, 1971.

[37] Z. Yasong and J. Guowei, "Study on properties of composites oxides TiO_2/SiO_2," *Chinese Journal of Chemical Engineering*, vol. 10, no. 3, pp. 349–353, 2002.

[38] A. A. Essawy, A. M. Nassar, and W. A. A. Arafa, "A novel photocatalytic system consists of Co(II) exhibits potent antimicrobial activity and efficient solar-induced wastewater remediation," *Solar Energy*, vol. 170, pp. 388–397, 2018.

[39] A. Kumar, A. Kumar, G. Sharma et al., "Quaternary magnetic BiOCl/g-$C_3N_4/Cu_2O/Fe_3O_4$ nano-junction for visible light and solar powered degradation of sulfamethoxazole from aqueous environment," *Chemical Engineering Journal*, vol. 334, pp. 462–478, 2018.

[40] S. Javaid, M. A. Farrukh, I. Muneer, M. Shahid, M. Khaleeq-ur-Rahman, and A. A. Umar, "Influence of optical band gap and particle size on the catalytic properties of Sm/SnO_2-TiO_2 nanoparticles," *Superlattices and Microstructures*, vol. 82, pp. 234–247, 2015.

[41] D. Li, H. Song, X. Meng et al., "Effects of particle size on the structure and photocatalytic performance by alkali-treated TiO_2," *Nanomaterials*, vol. 10, no. 3, p. 546, 2020.

[42] Q. Shi, Y. Zhang, D. Sun et al., "Bi_2O_3-sensitized TiO2Hollow Photocatalyst drives the efficient removal of Tetracyclines under visible light," *Inorganic Chemistry*, vol. 59, no. 24, pp. 18131–18140, 2020.

[43] T. Tang, Z. Yin, J. Chen et al., "Novel pn heterojunction Bi_2O_3/Ti^{3+}-TiO_2 photocatalyst enables the complete removal of tetracyclines under visible light," *Chemical Engineering Journal*, vol. 417, article 128058, 2021.

[44] S. L. Percival, P. G. Bowler, and J. Dolman, "Antimicrobial activity of silver-containing dressings on wound microorganisms using an in vitro biofilm model," *International Wound Journal*, vol. 4, no. 2, pp. 186–191, 2007.

[45] L. E. Brus, "A simple model for the ionization potential, electron affinity, and aqueous redox potentials of small semiconductor crystallites," *The Journal of Chemical Physics*, vol. 79, no. 11, pp. 5566–5571, 1983.

[46] M. Anpo, T. Shima, S. Kodama, and Y. Kubokawa, "Photocatalytic hydrogenation of propyne with water on small-particle titania: size quantization effects and reaction intermediates," *The Journal of Physical Chemistry*, vol. 91, no. 16, pp. 4305–4310, 1987.

[47] H. Lin, C. Huang, W. Li, C. Ni, S. Shah, and Y. Tseng, "Size dependency of nanocrystalline TiO_2 on its optical property and photocatalytic reactivity exemplified by 2-chlorophenol," *Applied Catalysis B: Environmental*, vol. 68, pp. 1–11, 2006.

[48] M. K. Rai, S. D. Deshmukh, A. P. Ingle, and A. K. Gade, "Silver nanoparticles: the powerful nanoweapon against multidrug-resistant bacteria," *Journal of Applied Microbiology*, vol. 112, no. 5, pp. 841–852, 2012.